

## Research Article

# One-Step Synthesized Pt-on-NiCo Nanostructures for Oxygen Reduction with High Activity and Long-Term Stability

Qiang Qu, Ming Wen, Mingzhu Cheng, Anwei Zhu, Biao Kong, and Yang Tian

Department of Chemistry, Tongji University, Siping Road 1239, Shanghai 200092, China

Correspondence should be addressed to Ming Wen, m.wen@tongji.edu.cn and Yang Tian, yangtian@mail.tongji.edu.cn

Received 5 September 2011; Revised 19 October 2011; Accepted 19 October 2011

Academic Editor: Boniface Kokoh

Copyright © 2012 Qiang Qu et al. This is an open access article distributed under the Creative Commons Attribution License, which permits unrestricted use, distribution, and reproduction in any medium, provided the original work is properly cited.

A novel particle-on-alloy nanomaterial has been designed and successfully synthesized for oxygen reduction (ORR) with high activity and long-term stability, in which well-isolated Pt nanoparticles are supported by amorphous NiCo nanoalloys. The Pt-on-NiCo nanostructures are prepared through the artificial active collodion membrane by one-step method, and experimental data reveals that Pt is isolated and spreads onto the amorphous NiCo nanosupport, and not only Pt but also Ni and Co are metallic in the Pt-on-NiCo nanostructures. The optimized Pt<sub>53</sub>-on-NiCo nanostructures show higher activities in both the onset potential and kinetic current density toward the ORR relative to the commercial Pt reference catalysts because the Pt-on-NiCo catalyst could lower the OH<sub>ad</sub>, which is considered to inhibit the ORR toward water. Meanwhile, Pt-on-NiCo nanostructures exhibit relatively long-term stability with only ~8% loss in electrochemical surface area (ECSA) for Pt.

## 1. Introduction

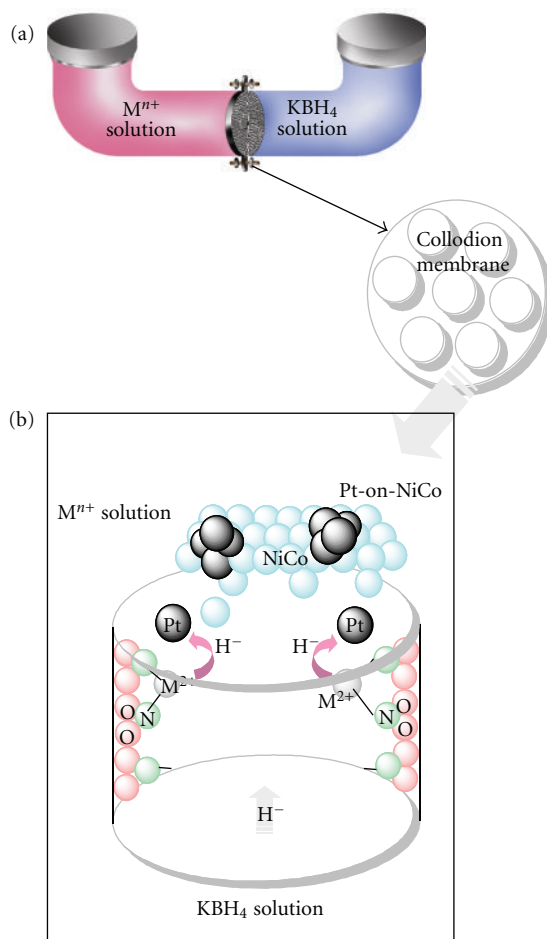
The electrocatalytic oxygen reduction (ORR) is one of the most important reactions in electrochemistry because it plays a vital role in electrochemical energy-conversion systems in fuel cells and metal-air batteries [1–9]. A large amount of efforts has been paid on development of efficient electrocatalysts. Platinum (Pt) is superior to many of the electrocatalysts investigated previously because of a direct four-electron reduction of O<sub>2</sub> at relatively low overpotentials. However, in the oxygen reduction reaction, the surface of the Pt catalyst tends to be shielded by the electrolyte or a hydroxyl layer [10]. As a result, the active sites on the Pt surface are reduced in number and the efficiency of the catalyst is limited. To improve the ORR activity, Pt catalysts have been alloyed with various nonprecious metals to reduce the binding strength between Pt atoms and the adsorbed species. Enhanced ORR activities of Pt alloyed with nonprecious metals such as Fe, Co, and Ni, have been reported in acid electrolyte solutions, though leaching of nonplatinum metal over time is a major problem [11–16]. The loss of surface area due to Ostwald ripening or grain growth is another major factor that often results in the degradation of catalytic performance. One solution to improve the durability is the

deposition of Au nanoclusters on Pt catalyst, another is Pt-on-Pd bimetallic nanostructures [17–24].

In our previous work, a series of amorphous nanoalloys, such as NiCo, FeNiPt and EuFePt, with different sizes and shapes have been successfully synthesized for enhanced electrocatalysis [25]. Herein, in order to improve both the activity and durability of electrocatalyst in oxygen reduction, we design a new particle-on-alloy nanostructured material, in which Pt nanoparticles are supported by an amorphous NiCo alloy. The Pt-on-NiCo nanostructures were synthesized through the artificial active templatecollodion membrane by one-step method, showing high electrocatalytic activity toward O<sub>2</sub> reduction. The optimized Pt<sub>53</sub>-on-NiCo nanostructures have improved both activity and stability of electrocatalyst for O<sub>2</sub> reduction, relative to the commercial Pt reference catalyst.

## 2. Experimental Section

**2.1. Chemicals and Materials.** Nickel chloride hexahydrate (NiCl<sub>2</sub>·6H<sub>2</sub>O, 98%), cobalt chloride hexahydrate (CoCl<sub>2</sub>·6H<sub>2</sub>O, 99%), dihydrogen hexachloroplatinate (H<sub>2</sub>PtCl<sub>6</sub>·6H<sub>2</sub>O, 99%), sodium hydroxide (NaOH, 96%), and potassium borohydride (KBH<sub>4</sub>, 95%) were purchased from



SCHEME 1: (a) Experimental setup for synthesis of Pt-on-NiCo nanostructures. (b) Proposed process for formation of Pt-on-NiCo nanostructures.

Sinopharm Chemical Reagent Co. Ltd. The organic solvent of ethanol ( $C_2H_5OH$ , 99.7%), n-hexanol ( $C_6H_{14}O$ ), and collodion solution ( $[C_6H_7O_2(OH)_{3-r}(ONO_2)_r]_n$  dissolved in ethanol and diethyl solvent) were purchased from Shanghai Lingfeng Chemical Reagent Co. Ltd. All the reagents were used without further purification. Pt reference catalysts for fuel cells with a diameter of 2.5 nm were purchased from E-TEK. Nafion solution (5 wt%) was received from Sigma and diluted with ethanol.

**2.2. Synthesis Method.** The preparation of collodion membrane within the thickness of about 0.18 mm was carried out on spin-coater (KW-4A, Chemat Technology) by using silicon substrate and collodion solution at the rotary speed of  $1000 \text{ r min}^{-1}$  for 15 s. Then the artificial active collodion membrane was treated in natural drying and peeling for spare. The Pt-on-NiCo nanostructures were synthesized through the experimental setup shown in Scheme 1. The collodion membrane was emplaced at the middle of the U-tube. 10 mL mixed solution of  $NiCl_2 \cdot 6H_2O$ ,  $CoCl_2 \cdot 6H_2O$ , and  $H_2PtCl_6 \cdot 6H_2O$  with a series of molar ratios was added into one side of U-tube, while 10 mL  $KBH_4$  solution with pH of 12 was added into the other side. After 1-2 days of

reaction, the black products were collected at the side of tube containing metal ions and thoroughly washed by distilled water and ethanol. Then the products were redispersed in ethanol for storage. In the present work, the amorphous NiCo alloy with the atom percent ratio of  $\sim 1:1$  was employed as a supporter for Pt catalysts with different atom percent contents (at.%), which were all characterized by area-scan EDX measurements. The Pt-on-NiCo nanostructures with Pt contents of at. X% were denoted as  $Pt_x\text{-on-NiCo}$ . The component contents of Ni, Co, and Pt are basically consistent with the starting molar ratios of  $Ni^{2+} : Co^{2+} : Pt^{4+}$ .

**2.3. Characterization.** The size and morphology of the catalysts were measured by using a high-resolution transmission electron microscope (HRTEM) (JEOL JEM-1200EX, Japan). The component analysis was carried out by the energy dispersive spectroscopy (EDS) using a Tecnai TF20 high-resolution transmission electron microscope (Oxford). The infrared (IR) spectrum was recorded on a Nicolet 560 FTIR spectrophotometer. The X-ray diffraction measurements were performed on a Bruker D8 (German) X-ray diffractometer using Cu K $\alpha$  radiation source ( $\lambda = 0.154056 \text{ nm}$ ). X-ray photoelectron spectroscopy (XPS) experiments were

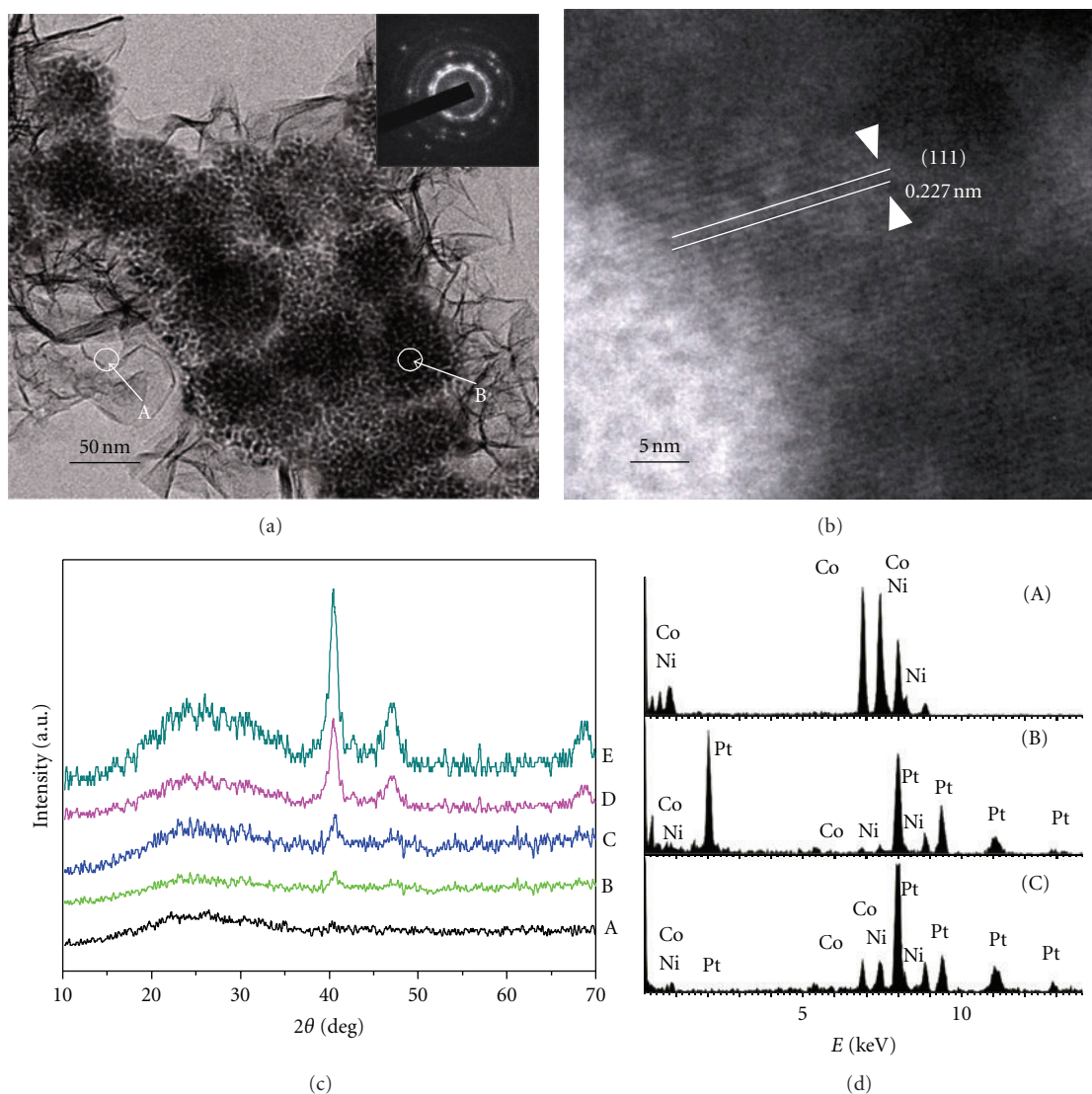


FIGURE 1: As-synthesized Pt-on-NiCo nanostructures: (a) TEM image; (b) HETEM image; (c) XRD patterns of (A)  $\text{Ni}_{50}\text{Co}_{50}$ , (B)  $\text{Pt}_5$ -on-NiCo, (C)  $\text{Pt}_{12}$ -on-NiCo, (D)  $\text{Pt}_{53}$ -on-NiCo, and (E)  $\text{Pt}_{71}$ -on-NiCo nanostructures; (d) In-situ EDX spectra in the area of (A) and (B), and area-scan EDX spectrum (C).

carried out on a RBD upgraded PHI-5000C ESCA system (Perkin Elmer) with Mg  $K\alpha$  radiation ( $h\nu = 1253.6$  eV). Binding energies were calibrated by using the containment carbon ( $\text{C } 1s = 284.6$  eV). For IR and XRD measurements, Pt-on-NiCo nanostructures were directly precipitated from ethanol solution. After drying at  $60^\circ\text{C}$  for 4 h in vacuum, the gel was ground into a powder for the measurements.

**2.4. Electrochemical Measurements.** Pt nanoparticles were purchased from E-TEK with a diameter of 2.5 nm. A suspension of 40 mg of carbon black (Vulcan XC72R) in 2 mL of ethanol was sonicated for 1 h, followed by the addition of 4 mg commercial Pt nanoparticles. The Pt-on-NiCo was only mixed with ethanol. A glassy carbon (GC) disk electrode (3.0 mm in diameter) was first polished with alumina slurries (1 and  $0.05\ \mu\text{m}$ , resp.) and then cleaned by sonication in Milli-Q water for about 5 min.  $4\ \mu\text{L}$  of

the dispersed catalyst was dropped onto the cleaned GC by a microliter syringe, followed by the addition of  $4\ \mu\text{L}$  of diluted Nafion (0.1 wt %) to form a thin film over the Pt-on-NiCo and Pt reference catalyst. The modified electrode was finally rinsed with excessive ethanol and Milli-Q water to remove loosely bound particles. Before recording the voltammograms, the modified surface was cleaned in  $\text{N}_2$ -saturated  $0.5\ \text{M H}_2\text{SO}_4$  by cycling between  $-0.2$  and  $1.3\ \text{V}$  (versus  $\text{Ag|AgCl}$ ) until the steady CVs were observed. Cyclic voltammetry and rotating disk voltammetry were performed using a computer-controlled CHI 760 electrochemical workstation (CH Instrument Company) and adjustable speed rotator (Pine Instrument Company). The electrochemical surface area (ECSA) was calculated by integrating the area under curve in the hydrogen adsorption range between 0.05 and  $0.4\ \text{V}$  for the backward sweep in the CV. The adsorption of hydroxyl species was calculated based on the  $\text{OH}_{\text{ad}}$  peak

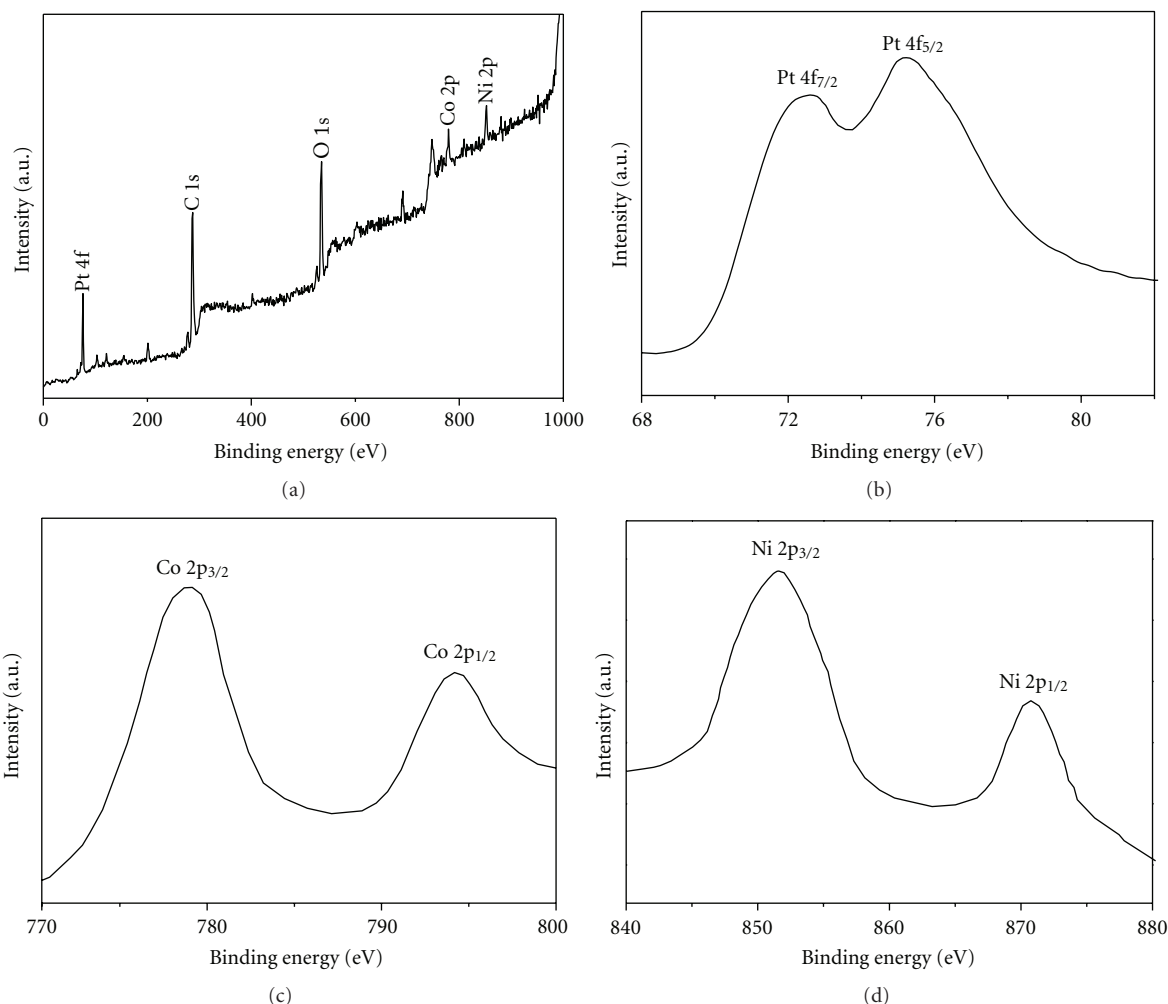


FIGURE 2: (a) XPS spectrum for  $\text{Pt}_{53}$ -on-NiCo nanostructures; detailed spectra for (b) Pt 4f, (c) Co 2p, and (d) Ni 2p in the  $\text{Pt}_{53}$ -on-NiCo nanostructures. The horizontal axis represents the binding energy corrected by that of C 1s.

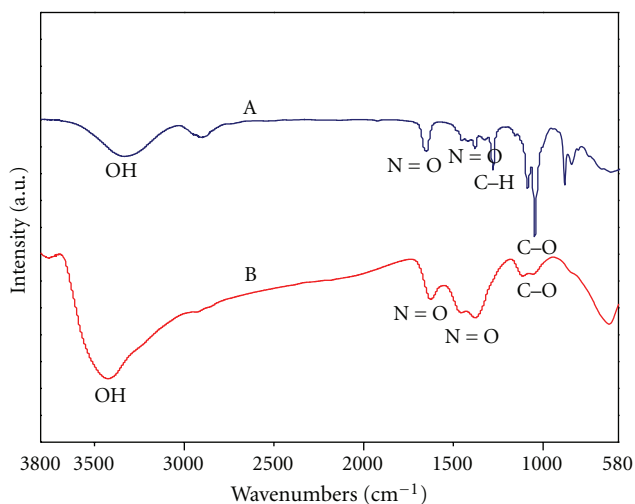


FIGURE 3: IR spectra recorded at (A) the collodion membrane and (B) the as-synthesized Pt-on-NiCo nanostructures.

in the CV curves at the potential larger than 0.6 V. Dividing the hydroxyl adsorption area by the overall active surface area resulted in the surface coverage of  $\text{OH}_{\text{ad}}$  species ( $\theta_{\text{OH}_{\text{ad}}}$ ). All oxygen reduction reaction (ORR) tests were conducted at ambient room temperature.

### 3. Results and Discussion

**3.1. Preparation and Characterization of Pt-on-NiCo Nanostructures.** The Pt-on-NiCo nanostructures were prepared through a one-step method using simple experimental setup shown in Scheme 1(a) employing one kind of artificial activity collodion membrane with a thickness of  $\sim 0.18$  mm as template. The hard template of collodion membrane was emplaced at the middle of U-tube. Mixed solution of  $\text{NiCl}_2 \cdot 6\text{H}_2\text{O}$ ,  $\text{CoCl}_2 \cdot 6\text{H}_2\text{O}$ , and  $\text{H}_2\text{PtCl}_6 \cdot 6\text{H}_2\text{O}$  was added into one side of U-tube with a series molar ratio, while  $\text{KBH}_4$  solution (pH 12.0) was added into the other side. The process for formation of Pt-on-NiCo nanostructures is illustrated in Scheme 1(b). Because the concentration

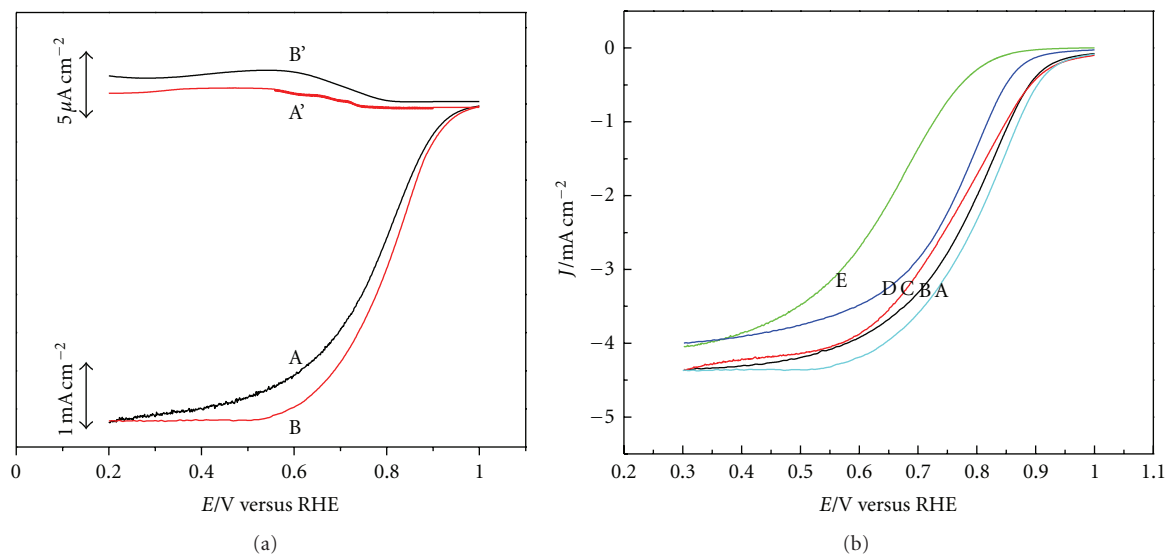


FIGURE 4: (a) Steady-state voltammograms for the ORR in  $\text{O}_2$ -saturated  $\text{HClO}_4$  (0.1 M) solution, at GCE-supported (A) Pt nanoparticles and (B)  $\text{Pt}_{53}$ -on-NiCo nanostructure surfaces. (b) Steady-state voltammograms for the ORR in  $\text{O}_2$ -saturated  $\text{HClO}_4$  (0.1 M) solution, at GCE-supported  $\text{Pt}_x$ -on-NiCo nanostructures surfaces with different Pt contents: (A) 53%, (B) 71%, (C) 23%, (D) 12%, and (E) 5%. Rotation rate: 200 rpm; potential was scanned at the disk electrode from 1.0 V to 0.0 V with scan rate of  $10 \text{ mV s}^{-1}$ . Curves A' and B' represent the corresponding Pt ring currents (polarized at 0.7 V).

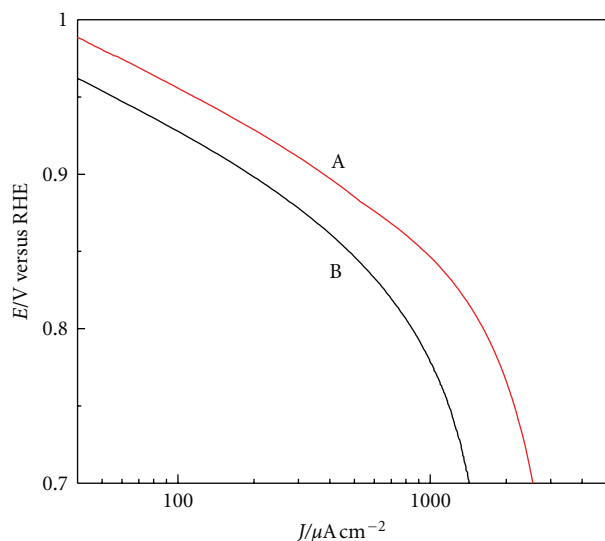


FIGURE 5: Tafel plots of kinetically controlled ORR currents extracted from Figure 4(a).

gradient of metal ions ( $M^{n+}$ ) and  $\text{H}^-$  generated from  $\text{BH}_4^-$  is formed at the interface of the colloid membrane and solution, either  $M^{n+}$  or  $\text{H}^-$  tends to diffuse toward the other side of membrane. The colloid membrane which composes of nitrocellulose with three-dimensional network has the capability to incorporate or to trap stably several kinds of active materials like fluorocarbon compounds. During the transfer process,  $M^{n+}$  cations ( $\text{Ni}^{2+}$ ,  $\text{Co}^{2+}$ , and  $\text{Pt}^{4+}$ ) rapidly coordinated to  $-\text{NO}_2$  groups on the pore-wall of colloid membrane and were reduced to metal atoms by

the passing  $\text{H}^-$  ions because of its strong reduction ability. The  $-\text{NO}_2$  groups may still surround the generated Pt-on-NiCo nanostructures, which will be demonstrated in detail later. Since the reduction potential of  $\text{Pt}^{4+}$  is much more positive than that of either  $\text{Ni}^{2+}$  or  $\text{Co}^{2+}$  and the atomic diameter of Pt is much greater than that of Ni or Co, Pt-on-NiCo nanostructures, not NiCoPt ternary alloys, are formed. In contrast, ultrathin nanofilms of NiCo amorphous alloys are produced when  $\text{Pt}^{4+}$  is absent.

Figure 1(a) shows TEM image of  $\text{Pt}_{53}$ -on-NiCo nanostructures, while TEM images of NiCo and other Pt-on-NiCo nanostructures with different contents (at.%) of Pt are also given in the Supplementary Material available online at doi: 10.1155/2011/842048 (Figure S1). It can be clearly observed that isolated Pt nanoparticles with diameter of  $\sim 5 \text{ nm}$  spread on the NiCo nanoalloys to form Pt-on-NiCo nanostructures. The selected-area electron diffraction pattern (SAED) for NiCo exhibits a diffuse halo (Figure S1a), corresponding to the chemical disorder of amorphous NiCo nanostructures. This observation was also confirmed by the broad peak at  $45^\circ$  for XRD pattern of the amorphous NiCo nanoalloys (Figure 1(c)A) [18]. However, SAED for  $\text{Pt}_{53}$ -on-NiCo nanostructures shows crystalline spot ring (inset in Figure 1(a)), which corresponds to the polycrystalline structure. This spot ring could be clearly observed even at  $\text{Pt}_{0.5}$ -on-NiCo nanostructures (SI, Figure S1b), indicating that Pt is isolated and spreads on the amorphous NiCo alloys, rather than alloyed with NiCo. The typical XRD patterns are shown in Figure 1(c). Unlike the broad peak for amorphous NiCo nanoalloy, the diffraction peaks of crystalline Pt (111) at  $40^\circ$  and (200)  $47^\circ$  can be clearly observed in the Pt-on-NiCo nanostructures, and the peak density increases with the increasing content of Pt. This also indicates that crystalline

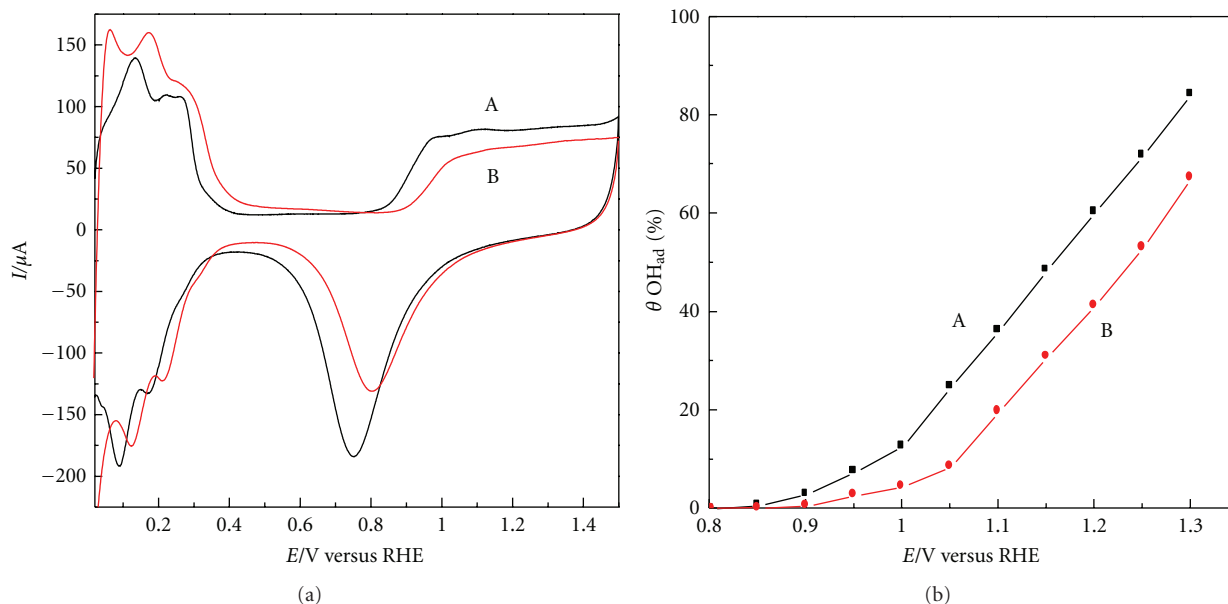


FIGURE 6: (a) CVs at GCE-supported (A) Pt nanoparticles and (B) Pt<sub>53</sub>-on-NiCo nanostructure surfaces in 0.5 M H<sub>2</sub>SO<sub>4</sub> solution purged with N<sub>2</sub>. Scan rate: 10 mV s<sup>-1</sup>. (b) Surface coverage of hydroxyl ( $\theta_{\text{OH}}$ ) calculated based on the corresponding OH<sub>ad</sub> formation region shown in (a).

Pt nanoparticles are isolated from amorphous NiCo support, which can be further confirmed by an HETEM image of Pt-on-NiCo nanostructure (Figure 1(b)). The lattice spacing of crystalline Pt is  $\sim 0.227$  nm and corresponds to (111) plane spacing of Pt crystal. Composition analysis is measured by in situ and area-scan energy dispersive X-ray analysis (EDX), as shown in Figure 1(d) and Figure S2. The in situ EDX spectra of Pt-on-NiCo nanostructures in area (A) and (B) almost agree with those of NiCo alloy and Pt, respectively, indicating again that Pt nanoparticles are isolated from NiCo nanoalloy. The area-scan EDX (C) and Figure S2 illustrating strong peaks of Ni, Co, and Pt undoubtedly confirmed that the products are NiCo and Pt-on-NiCo nanostructures.

XPS spectra for the Pt-on-NiCo nanostructures are presented in Figure 2, in which the numbers of emitted photoelectrons are given as a function of binding energy up to 1100 eV. Five photoemission peaks were clearly observed for Ni 2p, Co 2p, Pt 4f, C 1s, and O 1s, as shown in Figure 2(a), while the emission from the inelastic collisions of photoelectrons gave rise to a general background. The spectrum for Pt is depicted in Figure 2(b), two peaks located at 72.1 and 74.8 eV owing to the spin-orbit doublet splitting of 4f<sub>7/2</sub> and 4f<sub>5/2</sub> are in a good agreement with the values reported previously for metallic Pt [26]. In Figure 2(c), two peaks were clearly observed at 778.6 and 794.0 eV, respectively, which are ascribed to the multiplet splitting of 2p<sub>3/2</sub> and 2p<sub>1/2</sub> for Co(0). Two sharp peaks located at 851.8 and 870.7 eV, which are ascribed to the spin-orbit splitting of 2p<sub>3/2</sub> and 2p<sub>1/2</sub> for magnified Ni 2p, are demonstrated in Figure 2(d). The spin-orbit doublet splitting value of the 2p core level estimated to be  $\sim 18.9$  eV, corresponding to the difference of binding energies (BEs) between 2p<sub>3/2</sub> and 2p<sub>1/2</sub>, indicates that Ni(0) is dominant in the Pt-on-NiCo

nanostructures [27]. Thus, we can conclude that not only Pt but also Ni and Co are completely reduced and all of these metals are in their metallic state in the Pt-on-NiCo nanostructures.

Figure 3 shows the IR spectra recorded at (A) the collodion membrane and (B) the as-synthesized Pt-on-NiCo nanostructures. Several characteristic peaks located at 3430, 1620, 1380, and 1120 cm<sup>-1</sup> were clearly observed at the collodion membrane, in which the peaks located at 1620 cm<sup>-1</sup> and 1380 cm<sup>-1</sup> are assigned to the asymmetric and symmetric stretching vibration of the N=O bond, while the peaks observed at  $\sim 3430$  cm<sup>-1</sup> and  $\sim 1120$  cm<sup>-1</sup> are attributed to the asymmetric and symmetric stretching vibrations of the O-H and C-O bonds, respectively. The corresponding peaks ascribed to the stretching vibration of the N=O and C-O bonds were still obtained at the as-prepared Pt-on-NiCo nanostructures (curve B) although the intensities remarkably decreased. These observations suggest that the organic groups such as -NO<sub>2</sub> and -OH may surround the Pt-on-NiCo nanostructures and make them stable.

**3.2. Electrocatalytic Activity toward ORR.** The catalytic activity of the Pt-on-NiCo nanostructures toward ORR was evaluated in an electrochemical measurement system and compared with that of the commercial Pt reference catalyst for fuel cells (E-TEK). Steady-state hydrodynamic voltammetry with a rotating ring-disk electrode (RRDE) was employed to evaluate the intrinsic activities of catalysts on a glassy carbon electrode (GCE). Figure 4(a) shows hydrodynamic voltammograms recorded for the ORR at GCE disk-supported either Pt catalyst (curve A) or the optimized Pt<sub>53</sub>-on-NiCo nanostructures (curve B), with Pt

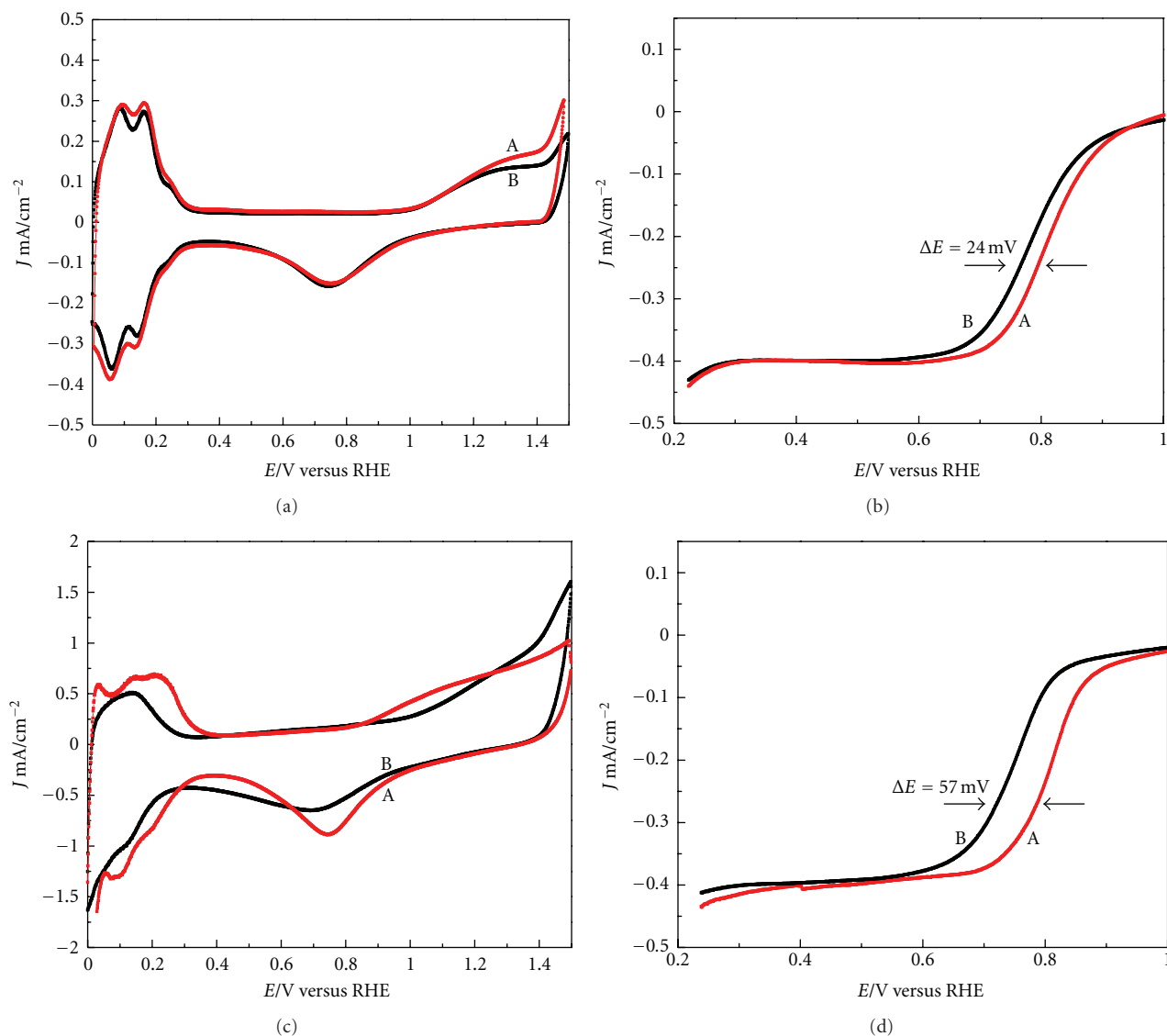


FIGURE 7: CVs (a) and (c) in 0.5 M  $\text{H}_2\text{SO}_4$  solution purged with  $\text{N}_2$  at scan rate of  $100 \text{ mV s}^{-1}$  and ORR polarization curves (b) and (d) in  $\text{O}_2$ -saturated  $\text{HClO}_4$  (0.1 M) solution at scan rate of  $10 \text{ mV s}^{-1}$  for GCE-supported (a) and (b)  $\text{Pt}_{53}$ -on-NiCo nanostructures and (c) and (d) Pt catalysts before (a) and after (b) 30,000 cycles.

ring electrodes in  $\text{O}_2$ -saturated  $\text{HClO}_4$  solution. The  $\text{Pt}_{53}$ -on-NiCo catalysts exhibited a more positive on-set potential ( $\sim 0.95 \text{ V}$ ) and high activity than other Pt-on-NiCo catalysts with different contents of Pt (Figure 4(b)) and the Pt reference catalyst. All the ring currents for catalysts arising from the oxidation of hydrogen peroxide generated at the individual disk electrodes were observed to be near zero, compared with the disk currents. According to the RRDE Equation [3],  $n = 4 - 2I_R / NI_D$ , where  $n$  is the electron number involved in the ORR,  $I_R$  the ring current,  $I_D$  the disk current, and  $N$  the collection efficiency of the RRDE. The electron number involved in the ORR by using the  $\text{Pt}_{53}$ -on-NiCo nanostructures and the commercial Pt catalyst was calculated to be  $\sim 4$ , indicating four-electron reduction of  $\text{O}_2$  to  $\text{H}_2\text{O}$  at all the catalysts. The area-specific current density

( $J_k$ ), which represents the intrinsic activity of the catalysts, was calculated using Koutecky-Levich equation [28]: as shown in Figure 5,  $J_k$  was estimated to be  $977 \mu\text{A cm}^{-2}$  Pt at  $0.85 \text{ V}$  for the  $\text{Pt}_{53}$ -on-NiCo nanostructures, which is near doubly large as that for the commercial Pt catalyst ( $493 \mu\text{A cm}^{-2}$ ). These results were in a good agreement with those obtained at Pt skin layers and Pt-on-Pd nanostructures [17, 29–32].

In order to find out the origin of the ORR enhancement by using Pt-on-NiCo catalysts, the cyclic voltammograms (CVs) of Pt-on-NiCo nanostructures and commercial Pt nanoparticles were measured in  $\text{HClO}_4$  solution under  $\text{N}_2$  bubbling, as shown in Figure 6(a). The CV peak associated with the formation of oxygenated adsorbates ( $0.8\text{--}0.9 \text{ V}$ ) at  $\text{Pt}_{53}$ -on-NiCo surface (curve B) was shifted to more anodic

potentials than that at Pt nanoparticles surface (curve A), suggesting the delayed formation of Pt oxides after the support by NiCo nanofilm [10]. By integrating the charge under the voltammograms of the Pt-on-NiCo and Pt surfaces, the fractional surface coverage for the adsorption of underpotentially deposited hydrogen and hydroxyl species was estimated. As shown in Figure 6(b), on Pt<sub>53</sub>-on-NiCo surface there is a clearly positive shift in OH<sub>ad</sub> formation (OH<sub>ad</sub>). As previously reported, the adsorbed OH<sub>ad</sub> species has a negative impact on the ORR toward water. Thus, the low OH<sub>ad</sub> coverage on the surface of Pt-on-NiCo nanostructures improves the kinetics of ORR, resulting in the higher activity toward ORR.

**3.3. Long-Term Stability.** The stability of the Pt-on-NiCo catalyst was evaluated by applying linear potential sweeps between 0.6 and 1.0 V as previously reported [17]. The electrochemical surface area (ECSA) was calculated by integrating the area under curve in the hydrogen adsorption range between 0.05 and 0.4 V for the backward sweep in the CV. The Pt<sub>53</sub>-on-NiCo nanostructures were observed to be quite stable with a loss of only ~8% initial ECSA (Figure 7(a)) and a small degradation of 5 mV in the half-wave potential (Figure 7(b)) after 30,000-cycles test. However, the commercial Pt catalyst lost ~26% of the initial ECSA as shown in Figure 7(c) and showed a large decrease of 28 mV in the half-wave potential after the same examination (Figure 7(d)). The stability of the present Pt-on-NiCo nanomaterial is better than that of the commercial Pt catalyst. The much developed stability may be ascribed to the large NiCo support of Pt catalyst and the presence of organic groups modified or/and surrounded by the Pt-on-NiCo nanostructures, which prevents the dissolution of small Pt nanoparticles on the NiCo nanofilm in the ORR process.

## 4. Conclusions

In summary, a new designed Pt-on-NiCo nanomaterial has been successfully developed by one-step method, in which Pt nanoparticles are supported by amorphous NiCo nanoalloy. The optimized Pt<sub>53</sub>-on-NiCo nanostructures show higher activities in both the onset potential and kinetic current density toward the ORR relative to the commercial Pt reference catalyst, because the new catalyst could lower the OH<sub>ad</sub>, which is considered to inhibit the ORR toward water. In addition, the support NiCo nanofilm and the organic groups modified or/and surrounded by Pt-on-NiCo nanostructures may prevent dissolution of the small Pt nanoparticles in the ORR, thus the present catalyst exhibits a long-term stability. This investigation opens up a novel way to designing the particle-on-alloy architectures for fuel cell catalysts with both excellent activity and stability.

## Acknowledgments

This work was financially supported by NSFC of China (20975075, 21175098, and 21171130), the National Basic

Research Program of China (2010CB912604), and Innovation Program of SECF (10ZZ21), 973 Project of China (2011CB93404).

## References

- [1] J. Zhang, K. Sasaki, E. Sutter, and R. R. Adzic, "Stabilization of platinum oxygen-reduction electrocatalysts using gold clusters," *Science*, vol. 315, no. 5809, pp. 220–222, 2007.
- [2] R. Partovi-Nia, B. Su, F. Li et al., "Proton pump for O<sub>2</sub> reduction catalyzed by 5,10,15,20-tetraphenylporphyrinato-cobalt(II)," *Chemistry: A European Journal*, vol. 15, no. 10, pp. 2335–2340, 2009.
- [3] M. S. El-Deab and T. Ohsaka, "Manganese oxide nanoparticles electrodeposited on platinum are superior to platinum for oxygen reduction," *Angewandte Chemie International Edition*, vol. 45, no. 36, pp. 5963–5966, 2006.
- [4] M. S. El-Deab, T. Sotomura, and T. Ohsaka, "Oxygen reduction at electrochemically deposited crystallographically oriented Au(1 0 0)-like gold nanoparticles," *Electrochemistry Communications*, vol. 7, no. 1, pp. 29–34, 2005.
- [5] I. Hatay, B. Su, F. Li et al., "Proton-coupled oxygen reduction at liquid-liquid interfaces catalyzed by cobalt porphine," *Journal of the American Chemical Society*, vol. 131, no. 37, pp. 13453–13459, 2009.
- [6] K. Gong, P. Yu, L. Su, S. Xiong, and L. Mao, "Polymer-assisted synthesis of manganese dioxide/carbon nanotube nanocomposite with excellent electrocatalytic activity toward reduction of oxygen," *Journal of Physical Chemistry C*, vol. 111, no. 5, pp. 1882–1887, 2007.
- [7] L. Mao, D. Zhang, T. Sotomura, K. Nakatsu, N. Koshiba, and T. Ohsaka, "Mechanistic study of the reduction of oxygen in air electrode with manganese oxides as electrocatalysts," *Electrochimica Acta*, vol. 48, no. 8, pp. 1015–1021, 2003.
- [8] J. Zhang, F. H. B. Lima, M. H. Shao et al., "Platinum monolayer on nonnoble metal-noble metal core-shell nanoparticle electrocatalysts for O<sub>2</sub> reduction," *Journal of Physical Chemistry B*, vol. 109, no. 48, pp. 22701–22704, 2005.
- [9] H. Yano, E. Higuchi, H. Uchida, and M. Watanabe, "Temperature dependence of oxygen reduction activity at nafion-coated bulk Pt and Pt/carbon black catalysts," *Journal of Physical Chemistry B*, vol. 110, no. 33, pp. 16544–16549, 2006.
- [10] V. R. Stamenkovic, B. Fowler, B. S. Mun et al., "Improved oxygen reduction activity on Pt<sub>3</sub>Ni(111) via increased surface site availability," *Science*, vol. 315, no. 5811, pp. 493–497, 2007.
- [11] H. Li, G. Sun, N. Li, S. Sun, D. Su, and Q. Xin, "Design and preparation of highly active Pt-Pd/C catalyst for the oxygen reduction reaction," *Journal of Physical Chemistry C*, vol. 111, no. 15, pp. 5605–5617, 2007.
- [12] X. Wang, J. Zhuang, Q. Peng, and Y. Li, "A general strategy for nanocrystal synthesis," *Nature*, vol. 437, no. 7055, pp. 121–124, 2005.
- [13] B. J. Hwang, S. M. S. Kumar, C. H. Chen et al., "An investigation of structure-catalytic activity relationship for Pt-Co/C bimetallic nanoparticles toward the oxygen reduction reaction," *Journal of Physical Chemistry C*, vol. 111, no. 42, pp. 15267–15276, 2007.
- [14] F. H. B. Lima, J. Zhang, M. H. Shao et al., "Catalytic activity—d-band center correlation for the O<sub>2</sub> reduction reaction on platinum in alkaline solutions," *Journal of Physical Chemistry C*, vol. 111, no. 1, pp. 404–410, 2007.
- [15] H. Yang, W. Vogel, C. Lamy, and N. Alonso-Vante, "Structure and electrocatalytic activity of carbon-supported Pt-Ni alloy

- nanoparticles toward the oxygen reduction reaction,” *Journal of Physical Chemistry B*, vol. 108, no. 30, pp. 11024–11034, 2004.
- [16] V. Raghuvver, P. J. Ferreira, and A. Manthiram, “Comparison of Pd-Co-Au electrocatalysts prepared by conventional borohydride and microemulsion methods for oxygen reduction in fuel cells,” *Electrochemistry Communications*, vol. 8, no. 5, pp. 807–814, 2006.
- [17] Z. Peng and H. Yang, “Synthesis and oxygen reduction electrocatalytic property of Pt-on-Pd bimetallic heteronanostructures,” *Journal of the American Chemical Society*, vol. 131, no. 22, pp. 7542–7543, 2009.
- [18] M. Wen, Y.-F. Wang, F. Zhang, and Q.-S. Wu, “Nanostructures of Ni and NiCo amorphous alloys synthesized by a double composite template approach,” *Journal of Physical Chemistry C*, vol. 113, no. 15, pp. 5960–5966, 2009.
- [19] M. Wen, D. Yang, Q.-S. Wu, R.-P. Lu, Y.-Z. Zhu, and F. Zhang, “Inducing synthesis of amorphous EuFePt nanorods and their comprehensive enhancement of magnetism, thermostability and photocatalysis,” *Chemical Communications*, vol. 46, no. 2, pp. 219–221, 2010.
- [20] M. Wen, Y.-Z. Zhu, Q.-S. Wu, F. Zhang, and T. Zhang, “Composition-dependent assembly and magnetic specificity of  $(\text{Fe}_{1-x}\text{Ni}_x)_{0.5}\text{Pt}_{0.5}$  amorphous nanothreads through substitution of Ni for Fe in an FePt system,” *Journal of Physical Chemistry C*, vol. 113, no. 46, pp. 19883–19890, 2009.
- [21] M. Arenz, T. J. Schmidt, K. Wandelt, P. N. Ross, and N. M. Markovic, “The oxygen reduction reaction on thin palladium films supported on a Pt(111) electrode,” *Journal of Physical Chemistry B*, vol. 107, no. 36, pp. 9813–9819, 2003.
- [22] N. Wakabayashi, M. Takeichi, H. Uchida, and M. Watanabe, “Temperature dependence of oxygen reduction activity at Pt-Fe, Pt-Co, and Pt-Ni alloy electrodes,” *Journal of Physical Chemistry B*, vol. 109, no. 12, pp. 5836–5841, 2005.
- [23] P. J. Ferreira, G. J. La O, Y. Shao-Horn et al., “Instability of Pt/C electrocatalysts in proton exchange membrane fuel cells: a mechanistic investigation,” *Journal of the Electrochemical Society*, vol. 152, no. 11, pp. A2256–A2271, 2005.
- [24] W. Chen, J. Kim, S. Sun, and S. Chen, “Electrocatalytic reduction of oxygen by FePt alloy nanoparticles,” *Journal of Physical Chemistry C*, vol. 112, no. 10, pp. 3891–3898, 2008.
- [25] M. Wen, H. Liu, F. Zhang et al., “Amorphous FeNiPt nanoparticles with tunable length for electrocatalysis and electrochemical determination of thiols,” *Chemical Communications*, no. 30, pp. 4530–4532, 2009.
- [26] X. Su, H. Zheng, Z. Yang, Y. Zhu, and A. Pan, “Preparation of nanosized particles of FeNi and FeCo alloy in solution,” *Journal of Materials Science*, vol. 38, no. 22, pp. 4581–4585, 2003.
- [27] W. B. Mi, H. Liu, Z. Q. Li, P. Wu, E. Y. Jiang, and H. L. Bai, “ $L1_0$  phase transformation and magnetic behaviors of (Fe, FePt, FePtCu)-C nanocomposite films,” *Journal of Applied Physics*, vol. 97, no. 12, Article ID 124303, 6 pages, 2005.
- [28] A. J. Bard and L. R. Faulkner, *Electrochemical Methods-Fundamentals and Application*, John Wiley & Sons, New York, NY, USA, 2nd edition, 2001.
- [29] V. R. Stamenkovic, B. S. Mun, M. Arenz et al., “Trends in electrocatalysis on extended and nanoscale Pt-bimetallic alloy surfaces,” *Nature Materials*, vol. 6, no. 3, pp. 241–247, 2007.
- [30] J. Zhang, M. B. Vukmirovic, K. Sasaki, A. U. Nilekar, M. Mavrikakis, and R. R. Adzic, “Mixed-metal Pt monolayer electrocatalysts for enhanced oxygen reduction kinetics,” *Journal of the American Chemical Society*, vol. 127, no. 36, pp. 12480–12481, 2005.
- [31] V. R. Stamenkovic, B. S. Mun, K. J. J. Mayrhofer, P. N. Ross, and N. M. Markovic, “Effect of surface composition on electronic structure, stability, and electrocatalytic properties of Pt-transition metal alloys: Pt-skin versus Pt-skeleton surfaces,” *Journal of the American Chemical Society*, vol. 128, no. 27, pp. 8813–8819, 2006.
- [32] J. L. Fernández, V. Raghuvver, A. Manthiram, and A. J. Bard, “Pd-Ti and Pd-Co-Au electrocatalysts as a replacement for platinum for oxygen reduction in proton exchange membrane fuel cells,” *Journal of the American Chemical Society*, vol. 127, no. 38, pp. 13100–13101, 2005.



**Hindawi**

Submit your manuscripts at  
<http://www.hindawi.com>

